1-1-2018

Porous ZrC-carbon microspheres as potential insoluble target matrices for production of $^{188}W/^{188}Re$

Nicholas Scales
Australian Nuclear Science And Technology Organisation, ns112@uowmail.edu.au

Jun Chen
University of Wollongong, junc@uow.edu.au

Robert Aughterson
Australian Nuclear Science And Technology Organisation

Inna Karatchevtseva
Australian Nuclear Science And Technology Organisation

Attila Stopic
Australian Nuclear Science And Technology Organisation

See next page for additional authors

Porous ZrC-carbon microspheres as potential insoluble target matrices for production of $^{188}W/^{188}Re$

Abstract

New microsphere sorbents are reported, which could find application in demanding radiation environments and especially as targets for the production of nuclear medicines by neutron irradiation. An easily-synthesized Zr anionic complex was introduced into quaternary amine-functionalised polystyrene-divinylbenzene-based anion-exchange resins by batch adsorption. Upon carbothermal reduction, the precursors were converted to porous carbon matrices containing particles of ZrC and ZrO2polymorphs. The most phase-pure material, ZrAX-1, possessed high surface area, multi-scale porosity and high mechanical strength. Adsorption of Re and W was investigated and its possible deployment as a reusable host for the production of188W/188Re is discussed.

Disciplines

Engineering | Physical Sciences and Mathematics

Publication Details

Scales, N., Chen, J., Aughterson, R. D., Karatchevtseva, I., Stopic, A., Lumpkin, G. R. & Luca, V. (2018).

Porous ZrC-carbon microspheres as potential insoluble target matrices for production of $^{188}W/^{188}Re$. Journal of Radioanalytical and Nuclear Chemistry: anÂ International Journal dealing with all AspectsÂ and Applications of Nuclear Chemistry, 318 (2), 835-847.

Authors

Nicholas Scales, Jun Chen, Robert Aughterson, Inna Karatchevtseva, Attila Stopic, Gregory R. Lumpkin, and Vittorio Luca

Porous ZrC-carbon microspheres as potential insoluble target matrices for production of $^{188}W/^{188}Re$

Nicholas Scales[a, *], Jun Chen[b], Robert D. Aughterson[a], Inna Karatchevtseva[a], Attila Stopic[a], Gregory R. Lumpkin[a] and Vittorio Luca[c]

[a]Australian Nuclear Science and Technology Organisation, Locked Bag 2001, Kirrawee DC, New South Wales, 2232, Australia

[b]Intelligent Polymer Research Institute, ARC Centre of Excellence for Electromaterials Science, Australian Institute of Innovative Materials, University of Wollongong, Innovation Campus, North Wollongong, NSW 2522, Australia

[c]Programa Nacional de Gestión de Residuos Radiactivos, Comisión Nacional de Energía Atómica, Centro Atómico Constituyentes, Av. General, Paz 1499, 1650 San Martin, Provincia de Buenos Aires, República Argentina

[*]Corresponding author (nsz@ansto.gov.au)

Abstract

New microsphere sorbents are reported, which could find application in demanding radiation environments and especially as targets for the production of nuclear medicines by neutron irradiation. An easily-synthesized Zr anionic complex was introduced into quaternary amine-functionalised polystyrene-divinylbenzene-based anion-exchange resins by batch adsorption. Upon carbothermal reduction, the precursors were converted to porous carbon matrices containing particles of ZrC and zirconia polymorphs. One material (ZrAX-1) contained substantially phase-pure ZrC and possessed high surface area, multi-scale porosity and high mechanical strength. Adsorption of Re and W was investigated and its possible deployment as a reusable host for the production of $^{188}W/^{188}Re$ was discussed.

Keywords

Zirconium carbide, 188Re, transmutation, microspheres, ion-exchange, carbonization

1 Introduction

Rhenium-188 ($\lambda_{1/2}$ = 17.0 hours) is an important radioisotope used for targeted radionuclide therapy. It possesses a high energy β-emission (2.11 MeV) well-suited to the annihilation of cancerous cells. Additionally, the accompanying γ-emission (155 keV) is convenient for real-time gamma camera imaging [1]. The ^{188}Re product can be labelled using various ligands to produce radiopharmaceuticals to target specific organs. For example, ^{188}Re-HEDP is used for palliative treatment of bone metastases [2].

The conventional synthesis route of ^{188}Re involves reactor-based neutron irradiation of ^{186}W-enriched oxide or metal targets. Double neutron capture results in formation of ^{188}W ($\lambda_{1/2}$ = 69.8 days) (Eq. 1). Typically, the ^{188}W-containing irradiated targets are subsequently dissolved in $NaOH/H_2O_2$ and loaded onto alumina generators, from which the sought-after but short-lived ^{188}Re product (Eq. 2) is conveniently eluted at point-of-use [3]. Owing to the long half-life of ^{188}W, the ^{188}W/^{188}Re generator has a long shelf-life, which is a considerable attribute [1].

$$^{186}W + 2n \rightarrow {}^{188}W + 2\gamma \quad (1)$$

$$^{188}W \rightarrow {}^{188}Re + \beta^- + \bar{\nu}_e \quad (2)$$

There is arguably room for improvement in the current scheme of irradiation and dissolution. Engineered porous and inert material targets could offer greater efficiency as well as the potential for reuse. However, such materials would be need to be highly resistant to radiation. Zirconium carbide (ZrC) is a refractory ceramic and interstitial compound crystallising in the NaCl-type cubic structure (space group Fm3m). It is well-suited to nuclear applications because of its high melting point, good thermal conductivity, excellent radiation tolerance and low neutron cross-section [4]. One possible application of ZrC, for example, is as a replacement coating for TRISO fuel particles [5]. In our earlier paper, we reported novel hierarchically porous carbon-ZrC spheres synthesised using carbothermal reduction of polyacrylonitrile (PAN) structural templates, Zr-doped using co-precipitation and infiltration methods [6]. We envisioned these materials as non-dissolvable and reusable transmutation

matrices, with porous granular structures facilitating column chromatography, allowing for the convenient adsorption of target species and elution of products post-irradiation. In the context of nuclear medicine production, these matrices could improve process efficiency, because the need for target dissolution post-irradiation would be eliminated; also, the recycle of some costly isotopically-enriched target nuclides would be facilitated, potentially reducing production costs. These could be readily recovered by adsorption and there would be no need for reconstitution.

In our recent publication, we reported an improved and facile synthetic route for the preparation of these kinds of porous composites, utilising ion-exchange for introduction of Zr into sulphonate-functionalised polystyrene-divinylbenzene cation-exchange resins, with the initial objective of synthesising the ZrC phase. While there were some expectations that S would volatilise at low temperature; instead, it was retained and the ternary MAX phase carbide, Zr_2SC, was obtained [7]. In the present work, we prospectively explore an anion-exchange route to prepare materials using S-free organic resins, to assure formation of ZrC. Specifically, we have synthesised the trisoxalatozirconate(IV) complex [8] for anion-exchange into quaternary amine-functionalised polystyrene-divinylbenzene resins.

The aims of this work were to produce novel carbon-ZrC composite microspheres using a simple ion-exchange procedure and subsequent carbothermal reduction; characterise their compositions and structures; and investigate their W and Re adsorption properties.

2 Experimental

2.1 Materials

All reagents, including anion-exchange resins, were used as received and without further purification. Amberlite® IRA-900 chloride form, Dowex® 22 chloride form, AMBERJET® 4200 chloride form, Dowex® 1X4 chloride form, $ZrOCl_2.8H_2O$ (98%), $(NH_4)_2C_2O_4.H_2O$ (>= 99%), $Na_2WO_4.2H_2O$ (>= 99%) were all sourced from Sigma Aldrich, Australia; while $NaReO_4$ (99.9%) was purchased from Strem Chemicals, USA. Analytical grade HCl (32%) and NaOH (50–52 wt%) solutions were sourced from Merck, Australia and Fluka Chemicals,

Australia, respectively. Instrument grade air and 3.5 mol% H_2-Ar gas mix were both supplied by Coregas, Australia. Milli-Q® high purity water (18.2 MΩ.cm) was used in all experiments.

2.2 Synthesis

Based on the method of Bochkarev et al. [8], a 0.05 mol L^{-1} Zr-oxalate aqueous solution, nominally ammonium trisoxalatozirconate(IV), $(NH_4)_2[Zr(C_2O_4)_3]$, was prepared by addition (10 mL increments) of 500 mL of 0.1 mol L^{-1} $ZrOCl_2$ solution, to 500 mL of 0.3 mol L^{-1} $(NH_4)_2C_2O_4$ solution, until all of the former was consumed. This was accomplished at room temperature in a large beaker using vigorous magnetic stirring. In some instances, the resulting solution was visibly turbid, in which case it was clarified with gentle heating (< 50 °C).

The materials fabricated were designated according to their precursors, which were all anion exchange resins based on a quaternary amine-functionalised polystyrene-divinylbenzene framework (detailed specifications are given in Table S1). Nomenclature was of the general form, *ZrAX-n*, where *Zr* indicates the sorbed metal, Zr; *AX* denotes anion exchange; and *-n* is an arbitrary and sequential natural number referring to the resin substrate. These were, namely, Amberlite® IRA-900 chloride form (ZrAX-1), Dowex® 22 chloride form (ZrAX-2), AMBERJET® 4200 chloride form (ZrAX-3) and Dowex® 1X4 chloride form (ZrAX-4). They were each loaded with the anionic Zr complex by contacting at a volume-to-mass ratio (*V*/*m*) of 50 mL g^{-1} for one day, with gentle agitation provided by a platform shaker (IKA, Germany). The loaded resins were collected under suction, thoroughly washed with Milli-Q® water and leached for one day with Milli-Q® water at *V*/*m* of 50 mL g^{-1} (with respect to original starting resin mass), also employing shaking. Finally, the leached solids were rinsed once more with a large excess of Milli-Q® water, air-dried overnight under suction and dried overnight in a vacuum oven at 60 °C (Thermo Electron, Germany).

Thermal treatment of the Zr-loaded anion exchange resins was conducted according to the conditions detailed in our previous work [6]. Briefly, carbothermal reduction was carried out in a tube furnace under a flow of 3.5 % H_2-Ar gas mix at a standard temperature of 1350 °C (unless indicated otherwise in the text) for 24 hours duration, employing a graphite foil-lined graphite boat and lid (featuring a 5 mm diameter hole for escape of gaseous products).

2.3 Characterisation

Thermogravimetric Analysis (TGA) was conducted using a Seiko Instruments Inc. EXSTAR6000 thermal analyser under instrument air carrier and with heating rates of 10 °C min^{-1}. Samples were vacuum-dried overnight at 100 °C prior to analysis and back-filled with N_2 to exclude air.

Power X-Ray Diffraction (XRD) was acquired with PANalytical X'pert Pro X-Ray Diffractometer using Cu weighted Kα radiation 1.5406 / 1.5444 Å 2:1, a step size of 0.0334 2θ° and an effective scan step time of 624.965 s. Samples were backed with single crystal silicon inserts cut off-axis. Rietveld analysis was performed with PANalytical X'Pert HighScore software Version 3.0. Backgrounds and profiles were fitted with shifted Chebyshev II polynomial and pseudo-Voigt functions, respectively.

The Zr, Hf and Cl concentrations in each thermally-treated microsphere sample was measured using Neutron Activation Analysis (NAA), which was conducted at the OPAL Research Reactor, Lucas Heights, Australia. Gamma spectra of samples were acquired with high purity Ge gamma detectors (P-type, 25% relative efficiency), following five minutes of neutron irradiation in a thermal neutron flux of 2.2×10^{13} cm^{-2} s^{-1}. The well-known k_0-method [9] and certified gold wires standards were employed for standardisation. The O and N concentrations were measured by microanalysis employing a LECO TCH600 instrument and a standard inert gas fusion method. Prior to analysis, the samples for both NAA and O, N microanalysis were vacuum-dried overnight at 100 °C in glass vials; back-filled with N_2; and tightly capped and sealed with plastic film.

Optical images of whole microspheres were taken with Wild M400 optical macroscope with no further sample preparation. Secondary electron images of Pt-coated (2–3 nm) fractured microsphere surfaces were acquired with a Zeiss Ultra Plus Scanning Electron Microscope (SEM). Scanning Transmission Electron Microscopy (STEM) images and Energy Dispersive Spectroscopy (EDS) spectra were acquired using a JEOL 2200FS operated at 200 keV. Specimens were crushed, suspended in ethanol and dispersed on holey carbon films, supported on TEM Cu mesh grids.

A Micromeritics ASAP 2020 surface area and porosity analyser was used for acquisition of nitrogen adsorption-desorption isotherms at 77 K (−196 °C). Samples were vacuum-degassed at 150 °C. The total surface areas were calculated using the Brunauer-

Emmett-Teller (BET) equation; micropore and external surface areas, using a t-plot method; and a Density Functional Theory (DFT), N_2 on carbon slit pore model, was used to derive pore size distributions.

A Renishaw inVia™ Raman spectrometer fitted with a Peltier-cooled CCD detector was used to acquire Raman spectra, utilising either argon (514 nm) or HeCd (325 nm) laser excitation. Calculations of carbon in-plane crystallite size was performed using a general expression (Eq. 3) accounting for the laser wavelength:

$$L_a = (2.4 \times 10^{-10})\lambda_{laser}^4 \left(\frac{I_D}{I_G}\right)^{-1} \quad (3)$$

where L_a is the in-plane crystallite size (nm), λ_{laser} is the laser wavelength (nm), I_D is the D peak intensity and I_G is the G peak intensity [10].

Mechanical strength testing of single microspheres was performed using an Instron 5967 instrument equipped with 500 N load cell. The testing configuration consisted of two metal flats (load cell and stationary surface). The compression rate was 0.01 mm min^{-1}.

2.4 Adsorption studies

For pH dependence studies, an aqueous stock solution containing $NaReO_4$ and Na_2WO_4, 1 mg L^{-1} with respect to both Re and W, was prepared by dissolution of the parent salts in Milli-Q® water. This solution was pH adjusted with either aqueous HCl or NaOH, employing magnetic stirring and subsamples of different pH were taken. The various pH solutions were aged for about a day and their final pH values measured.

For capacity measurements and loading of materials for STEM-EDS, single-element solutions 100 mg L^{-1} W (pH 3) and 25 mg L^{-1} Re (pH 5), respectively were prepared by dissolution of $Na_2WO_4.2H_2O$ and $NaReO_4$ salts in Milli-Q® water. The pH of each solution was adjusted by addition of aqueous HCl, accompanied by magnetic stirring. Both solutions were aged for one day before use and the absence of significant pH changes verified.

Adsorption experiments were executed by contacting the appropriate adsorbate solution with the microsphere material under batch contact conditions and with gentle agitation provided by a platform shaker (IKA, Germany). For pH dependence, samples were contacted in triplicate at a volume-to-mass (V/m) ratio of 200 mL g^{-1} and with a three day

contact time. For capacity, single solids were contacted at *V*/*m* of 50–1000 mL g^{-1} and four days were allowed for equilibrium; For loading of STEM-EDS specimens, *V*/*m* of 2000 mL g^{-1} and a four day contact time were used. Stocks and supernatants were diluted and analysed for Re and W with an Agilent 7900 ICP Mass Spectrometer. Values of % extraction were calculated using Eq. 3:

$$Extraction\ (\%)\ = \frac{C_i - C_e}{C_i} \times 100 \tag{3}$$

and uptakes were calculated with Eq. 4:

$$q_e = \frac{(C_i - C_e)V}{m} \tag{4}$$

where C_i is initial concentration (mg L^{-1}), C_e is equilibrium concentration (mg L^{-1}), q_e is the equilibrium amount adsorbed (mg g^{-1}), *V* is volume (L) and *m* is mass of sorbent (g). Triplicates (where applicable) were averaged and errors estimated from two sample standard deviations of each triplicate set. Details of standard calculations for fitting adsorption isotherm models are given in Supplementary Material.

3 Results and discussion

3.1 Loading of resins and effect of thermal treatment

The Zr loadings in the unheated resin precursors were confirmed by way of TGA in air, demonstrating refractory content of 10–18 wt%, presumed to be ZrO_2 (Table 1; the TGA plots are given in Fig. S1). Carbothermal reduction of the anion-exchanged resin precursors had the effect of generating highly-spherical and lustrous black microsphere products; ZrAX-1, representative of the series, is depicted (Fig. 1; all images of materials before and after thermal treatment are given in Fig. S2). The surface areas of the same materials varied considerably, ranging from 75–448 $m^2\ g^{-1}$ (Table 1). Material ZrAX-1, with the highest surface area, was also the material possessing the highest Zr loading in its precursor.

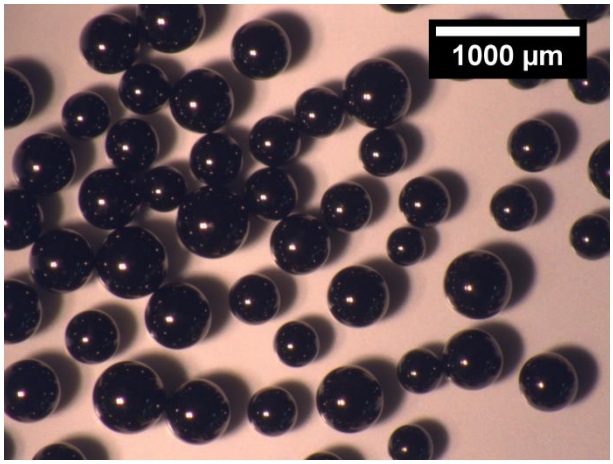

Figure 1 Optical image of ZrAX-1.

Table 1. Refractory residues obtained from TGA of unheated Zr-loaded anion-exchange resins; and corresponding BET surface areas of 1350 °C-heated products.

Material	*Residue (%)*	*BET surface area (m^2 g^{-1})*
ZrAX-1	17.8	448
ZrAX-2	12.3	75
ZrAX-3	10.8	139
ZrAX-4	10.7	135

3.2 Porosity

The internal pore structures of the microspheres were examined with SEM. The IUPAC recommendations define three pore size regimes; micropores (< 2 nm), mesopores (2–50 nm) and macropores (>50 nm) [11]. At low magnification, the inner texture of ZrAX-1 (Fig. 2a) was quite smooth, demonstrating the absence of large macropores (e.g. of the order of hundreds of micrometers); while at higher magnification (Fig. 2b), a coral-like porous texture was observed, which could be interpreted to be a mixture of large mesopores and small macropores. While ZrAX-2 to -4 (Fig. 2c–h) were also shown to lack large macropores, at higher magnification the surfaces textures exhibited some roughness and loose fragments which might be attributed to sample preparation, but with little or no porosity evident.

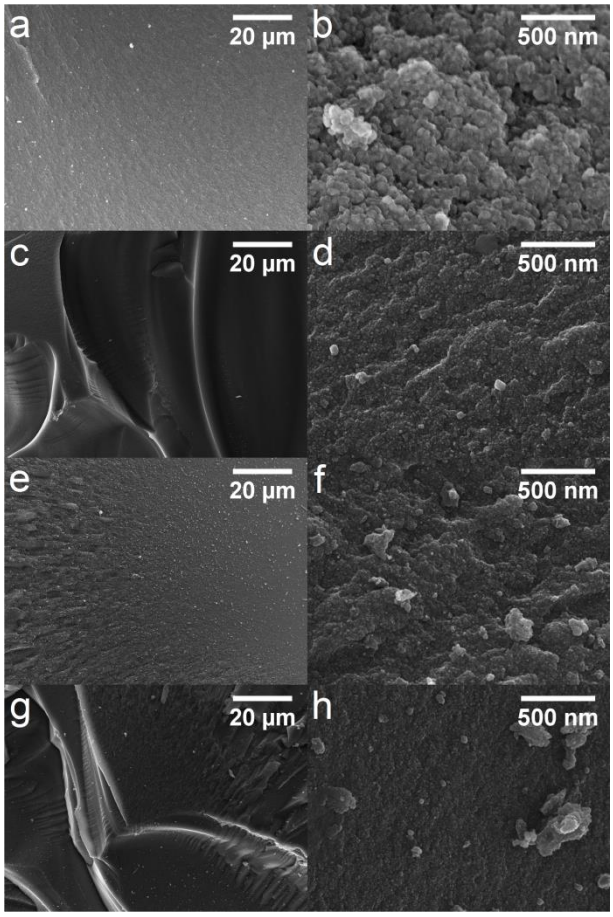

Figure 2 SEM images of internal fractured microsphere surfaces at 1,000 and 50,000 × magnification. (a) and (b) ZrAX-1; (c) and (d) ZrAX-2; (e) and (f) ZrAX-3; (g) and (h) ZrAX-4.

Further examination of the materials using Nitrogen Porosimetry revealed combinations of Type I and IV isotherm shapes (Fig. 3) according to the IUPAC classification [11], indicative of micro- and mesoporosity, respectively. For ZrAX-1 (Fig. 3a), these features are evident from the low pressure knee at low P/P_0 (Type I); and the conspicuous double hysteresis loop (Type IV). Significantly, the desorption branch showed a very flat plateau at P/P_0 approaching unity, signalling complete pore filling, as opposed to a Type II isotherm shape which would indicate presence of large macropores. The latter result is thus in agreement with the SEM data presented earlier. Materials ZrAX-2 to -4 (Fig. 3a; the isotherms are also plotted separately in Fig. 3b for clarity) also demonstrated Type I/IV hybrid isotherms, with each notably exhibiting poor hysteresis closure.

Pore size distributions are presented in Fig. 3c. The Pore size distribution of ZrAX-1 was trimodal, with micropores, small mesopores and a third and larger mesopore mode

extending just into the macropore regime. While Nitrogen Porosimetry is not usually applicable to large macropores, taken together with the earlier SEM observations, the overall picture is that ZrAX-1 is in fact tetramodal. The other three materials (ZrAX-2 to -4) could be broadly described as bimodal, containing micropores and small mesopores. Once again, the Nitrogen Porosimetry results have corroborated the SEM data.

In summary, the SEM and Nitrogen Porosimetry data together indicate the presence of multi-scale porosity in the microsphere materials and most notably in ZrAX-1. Hierarchical or multi-scale porosity is desirable for column chromatographic applications.

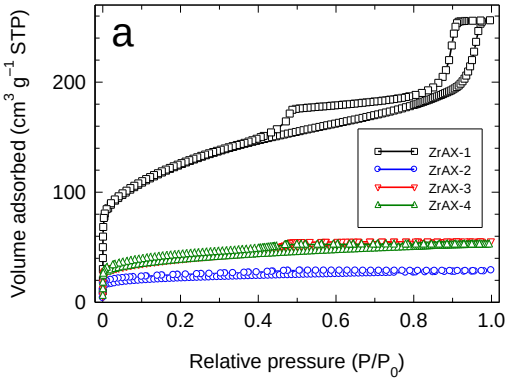

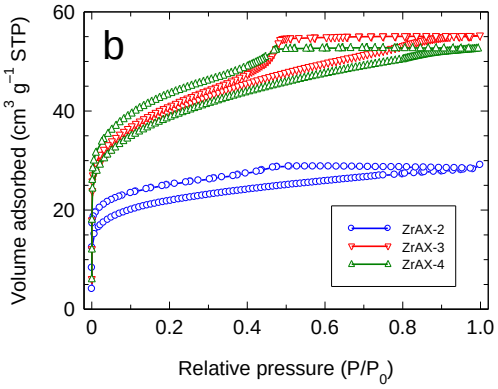

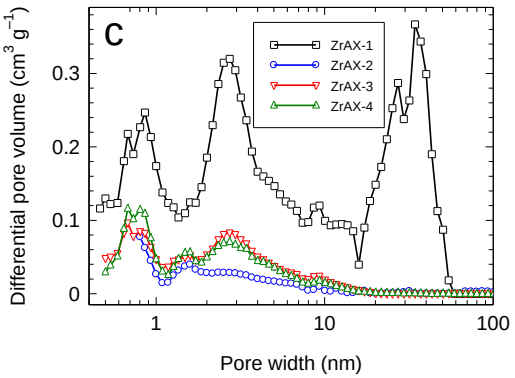

Figure 3. Nitrogen Porosimetry data. (a) and (b) nitrogen adsorption-desorption isotherms; and (c) pore size distributions.

3.3 Composition and chemical structure

Compositional analysis by NAA of the thermally-treated microspheres (Table 2) broadly corroborated the relative Zr loadings in the precursors determined by TGA, although Zr does appear to be well-concentrated by the thermal processing, suggesting considerable loss of carbonaceous material. Some Hf impurity in Zr was observed, as well as small quantities of Cl. The Cl content was considerably lower in the macroporous resin-derived ZrAX-1, compared with the gel resin-derived materials (ZrAX-2 to -4). The ion-exchange resins were all obtained in their chloride forms. The O content of the materials suggested the presence of some unreacted material, ZrO_2, or O dissolved in the carbide lattice. The O concentration in ZrAX-1 was considerably lower than those of the others, indicating more efficient conversion to ZrC. For the suite of materials, N concentrations were all relatively constant (0.34–0.46%). The C concentrations (inferred by difference), were all relatively similar for ZrAX-2 to -4 (53–61%) and thus C was the major constituent in each case. For ZrAX-1, however, C was much lower at *ca.* 38 wt%.

Table 2 Elemental compositions of the 1350 °C heated materials.

Material	*Zr (wt%)*	*O (wt%)*	*Hf (wt%)*	*N (wt%)*	*Cl (wt%)*	*Balance (wt%)*
ZrAX-1	52 ± 4	7.59 ± 0.15	1.18 ± 0.04	0.34	0.00179 ± 0.00015	38 ± 4
ZrAX-2	27.5 ± 1.9	10.0 ± 0.2	0.58 ± 0.04	0.46	0.132 ± 0.009	61 ± 2
ZrAX-3	32 ± 2	10.6 ± 0.2	0.73 ± 0.05	0.39	0.50 ± 0.03	55 ± 3
ZrAX-4	34 ± 2	11.0 ± 0.2	0.74 ± 0.05	0.34	0.45 ± 0.03	53 ± 3

Characterisation of the crystalline content of the various microsphere materials was undertaken; powder XRD patterns and their Rietveld fits are given in Fig. 4. The results of the Rietveld analysis are presented in Table 3. Material ZrAX-1, based on a macroporous resin substrate, was ostensibly phase-pure ZrC from a cursory inspection its XRD pattern and this was confirmed by the Rietveld. The remaining materials (ZrAX-2 to -4) were obviously mixtures of ZrC and ZrO_2 polymorphs. Each of the three contained tetragonal ZrO_2 ($tZrO_2$) (71.4–83.4%), a minor quantity of ZrC (11.9–17.3%), while ZrAX-2 also exhibited peaks identified as monoclinic ZrO_2 ($mZrO_2$) (16.6%).

According to the review of Katoh and co-workers, the ZrC cell dimension is related to the Zr/C stoichiometry. Based on the measured ZrC unit cell parameters (4.6746– 4.6895 Å), the ZrC phase is inferred to be $ZrC_{0.5}$.

Some interesting correlations can be drawn between the crystalline content of the materials and other previously measured characteristics. First, ZrAX-1 possessed macroporosity, while the other materials were mesoporous; second, the Cl content of ZrAX-1 was much lower than those of the other materials; and third, ZrAX-1 possessed a much higher Zr loading than the other three materials. These apparent connections could suggest a couple of possible explanations for the variation in ZrC conversion efficiency. One the one hand, the high phase purity of ZrAX-1 and its very low Cl content suggests that an open porous structure aided in the effective removal of O and formation of the ZrC phase. On the other hand, the correlation between high Zr loading and ZrC phase purity could indicate that a high density of Zr atoms on the resin is necessary for efficient conversion to ZrC.

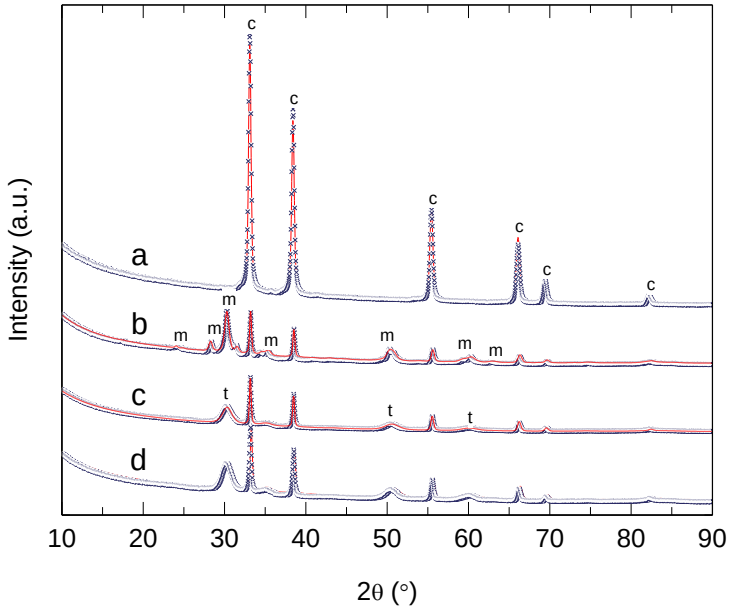

Figure 4. Powder XRD patterns and Rietveld fits, (a–d): ZrAX-1 to -4. Key: c, cubic phase, ZrC; m, monoclinic phase, ZrO_2; t, tetragonal phase.

Table 3. Rietveld analysis.

Material	*Phase*	*%*	*a (Å)*	*b (Å)*	*c (Å)*	*β (°)*	*vol (Å^3)*
ZrAX-1	ZrC	100	4.6895	4.6895	4.6895		103.1278
ZrAX-2	ZrC	11.9	4.6746	4.6746	4.6746		102.1471
	$tZrO_2$	71.4	3.5906	3.5906	5.1866		66.8668
	$mZrO_2$	16.6	5.1254	5.0875	5.4609	98.6774	140.7666
ZrAX-3	ZrC	17.3	4.6805	4.6805	4.6805		102.5335
	$tZrO_2$	82.7	3.5987	3.5987	5.1437		66.6145
ZrAX-4	ZrC	16.6	4.6795	4.6795	4.6795		102.4693
	$tZrO_2$	83.4	3.5998	3.5998	5.1362		66.5594

The most promising material of the series, ZrAX-1, was characterised by Raman Spectroscopy (Fig. 5) to gain insight into the nature of the carbon framework. Somewhat similar results to our earlier work were obtained [7]. The 325 nm near-UV spectrum provided evidence for absence of sp^3-hybridised carbon, due to the lack of T (tetrahedral) peak expected at 1060 cm^{-1}. However, both the 325 and 514 nm laser excitation spectra exhibited

features indicative of a ringed sp^2 carbon structure, i.e., a G (graphite) peak and D (disorder) peak. Along with the D peak dispersion (i.e. change in peak position as a function of excitation wavelength), which is seen in all carbon-based materials, a slight dispersion of the G peak possibly indicated a degree of structural disorder [12]. Contrasting our earlier results, however, this sample exhibited heating from the Raman laser, giving a broad hump at high wavenumbers obscuring the 2D overtone peak. The 2D overtone peak, found in this region (~2700 cm^{-1}), can yield information on the stacking order of the carbon crystallites [10]. However, in this instance, no comment can be made on the overtone peak and its implication for stacking or structural ordering of carbon crystallites.

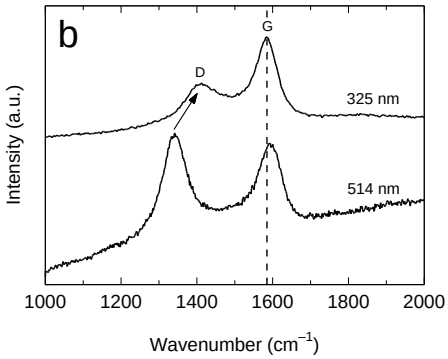

Figure 5. Raman spectra for ZrAX-1.

3.4 Mechanical stability

Material ZrAX-1 was evaluated for mechanical strength by a compressive testing regime performed on single microspheres. A representative compression versus load profile is given in Fig. S3. The average failure point was 19.2 N, with a sample standard deviation of 7.1 N (n = 10). For comparison, 1 N is equivalent to the weight exerted by a mass of 0.102 kg in Earth's gravity (a = 9.81 m s^{-2}). Therefore, the mechanical strength of this material should be more than sufficient for column use.

3.5 Structural evolution with temperature

Investigations of the temperature dependent structural evolution of ZrAX-1 were undertaken (Fig. 6). Powder XRD data is presented in Fig. 6a. At the lowest investigated temperature (850 °C), $tZrO_2$ was already fully-formed. By 1150 °C, the peak intensities of $tZrO_2$ had begun to decrease and faint peaks of ZrC were noticeable. At 1250 °C, the ZrC peaks predominated and by 1350 °C, the $tZrO_2$ peaks had all but disappeared.

The associated surface area changes were monitored (Fig. 6b; the corresponding adsorption-desorption isotherms are given in Fig. S4). Total (BET) surface area stayed relatively constant from 850 to 1050 °C, but then rapidly increased with temperature. At the lowest temperature of 850 °C, microporosity comprised the majority of the BET surface area. Above 1050 °C, the t-plot micropore surface area noticeably decreased with increasing temperature, while the external surface area (including mesoporosity) increased. These changes can be even more clearly seen in the pore size distribution data (Fig. 6c). At 850 °C, the distribution was basically bimodal with a moderate-sized micropore peak and a large mesopore peak. With increasing temperature, in-growth of a new micropore peak can be seen, which simultaneously shifted towards higher pore widths. By 1150 °C, this new mode had crossed the mesopore threshold (2 nm). Interestingly, this porosity development is similar to that presented in our recent work, however in that instance, micropores were formed instead of mesopores [7].

Raman measurements of these same specimens permitted the calculation of in-plane carbon crystallite sizes (Fig. 6d). The trend in this data was a decrease in the crystallite size as a function of temperature.

In our recent publication, we had argued that the appearance of micropores was attributable to reactive carbon removal and the present data would seem to support this as well. Some observable changes in surface area and porosity (850–1050 °C) precede the changes in crystallinity and formation of the ZrC phase. Also, the appearance of mesopores would seem to be at the expense of the carbon in-plane crystallite size; thus it is likely that the evolved high surface areas are the result of porosity formation in the carbon phase.

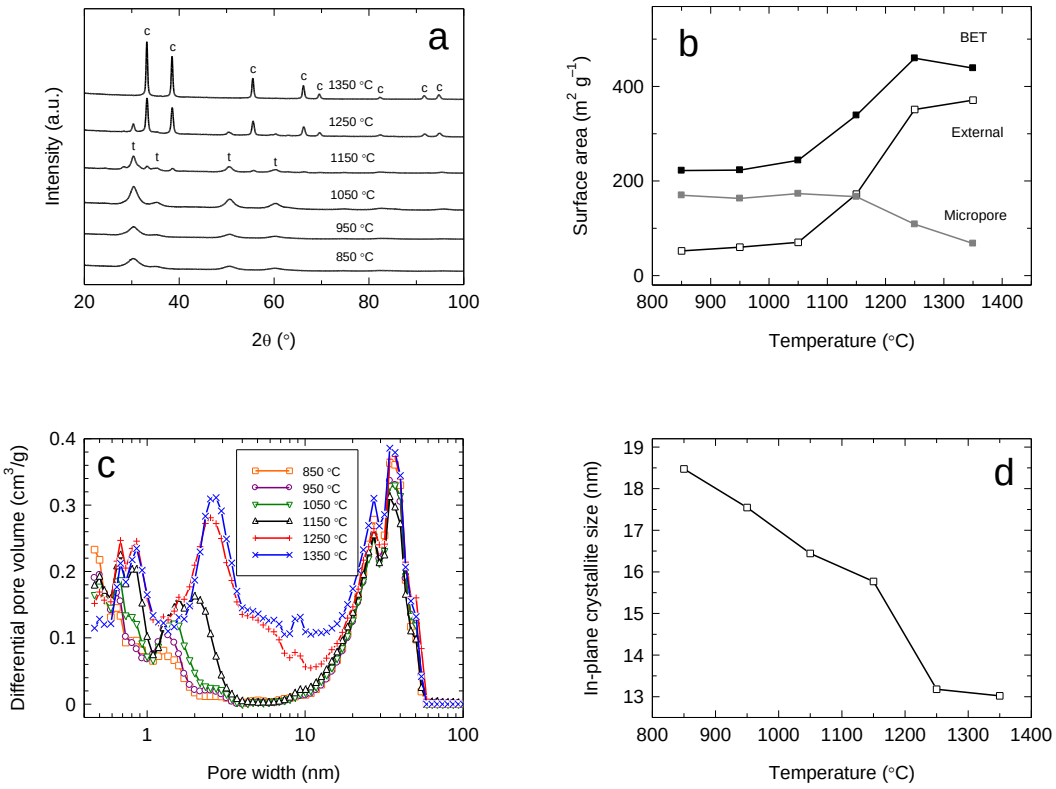

Figure 6 Structural evolution of ZrAX-1 as a function of temperature. (a) Powder XRD patterns. Key: c, (cubic) ZrC; t, (tetragonal) $tZrO_2$. (b) Surface areas. (c) DFT pore size distributions. (d) In-plane carbon crystallite sizes.

3.6 Adsorption studies

To illustrate the possible use of the microsphere materials as targets, $^{188}W/^{188}Re$ production was considered; adsorption of Re and W in sorption experiments were undertaken for ZrAX-1, employing cold (non-radioactive) and natural abundance isotopic source materials. Study of the adsorption of these elements as a function of pH was pertinent, given that ^{186}W is the target nuclide and ^{188}W is the irradiation product; and ^{188}Re is the desired product of ^{188}W decay. Both elements were observed to adsorb nearly quantitatively over a wide range of pH (Fig. 7), although seemingly, there was competition with OH^- at high pH. Of the two, Re was bound more strongly; non-quantitative adsorption of W was only observed at around pH 12.

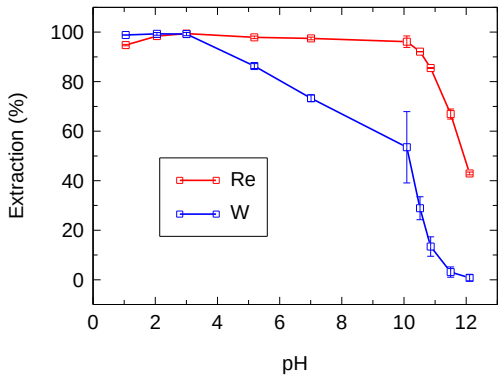

Figure 7 Adsorption pH dependence of ZrAX-1 for Re and W.

To assess adsorption capacities, adsorption isotherms for both Re at pH 5 (Fig. 8a) and W at pH 3 (Fig. 8b) onto ZrAX-1, were acquired and fitted with the Langmuir and Freundlich adsorption models. Model fit parameters are given in Table 4. The Langmuir fits were reasonable for both adsorbates. For Re, the Freundlich fit was marginally-better. The q_{max} values (Langmuir adsorption capacities) for Re and W were 11.06 and 49.54 mg g^{-1}, respectively. Re(VII) is believed to exist universally as the mononuclear ReO_4^- species. In contrast, the tendency of W(VI) towards cluster chemistry is well-known; at equilibrium, the dodecanuclear species, $W_{12}O_{39}^{6-}$, is expected to predominate under the conditions employed (pH 3 and 100 ppm concentration); however, equilibrium is only reached after many days. Hexanuclear clusters form quite rapidly though [13]. The W-to-Re ratio, which was therefore expected to be six-to-one, in practice was only approximately 4.5-to-one when measured. This shortfall in W capacity might be attributed to steric effects; that is, the W clusters are likely to occupy a larger footprint on the surface of the material. The high W loading is promising as it would permit ^{188}W to be produced in high yield. Based on the W adsorption capacity, assuming 100% enrichment of ^{186}W in the target material and total conversion to ^{188}W, it is calculated that up to 18 TBq (~500 Ci) of ^{188}W per gram of sorbent could theoretically be produced. For comparison, a typical ^{188}W generator is 37 GBq or 1 Ci [1].

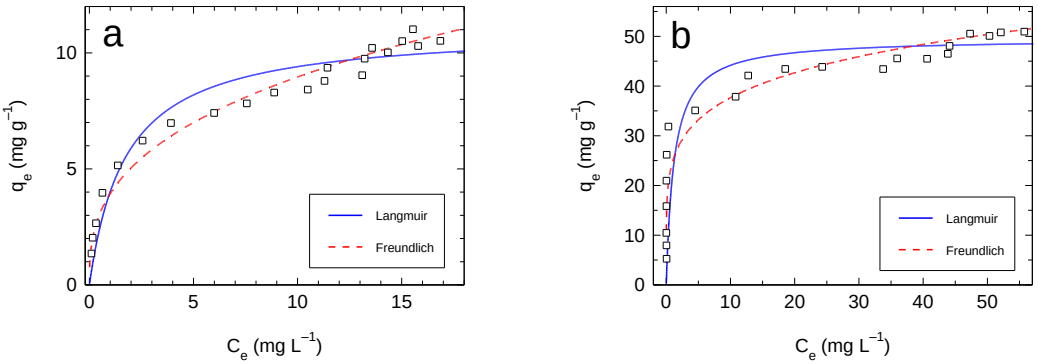

Figure 8 Isotherm adsorption data for ZrAX-1. (a) Re and (b) W, with Langmuir and Freundlich model fits.

Table 4 Isotherm model fit parameters for Re and W adsorption onto ZrAX-1.

Element	*Model*	q_{max} *(mg g^{-1})*	*b (L mg^{-1})*	*n*	K_f *(mg g^{-1})*	R^2
Re	Langmuir	11.06	0.571			0.974
	Freundlich			2.80	3.94	0.976
W	Langmuir	49.54	0.821			0.993
	Freundlich			5.54	24.85	0.771

In our recent paper, it was demonstrated that ReO_4^- accumulates upon the Zr_2SC phase [7]. In light of the Re and W adsorption data in the present work, we have used similar STEM-EDS elemental mapping methods to further investigate the Re and W adsorption upon the ZrAX-1 material. In the Re-loaded specimen (Fig. 9), dark particles of the ZrC phase can be seen against the lighter-shaded carbonaceous material (Fig. 9a). The elemental maps (Fig. 9b–e) showed that while C is found throughout the material and is somewhat concentrated within the discrete particles, the other elements (Zr, O and Re) were all coincident with these same particles. Thus, it can be said with certainty that the particles are of the ZrC phase and that Re adsorbs upon them, with little or no adsorption upon the carbonaceous phase. Comparable results were obtained for the W-loaded variant of ZrAX-1 (Fig. 10). Correlating the bright field image of the materials (Fig. 10a) with the elemental maps (Fig. 10b–e), Zr, O and W were once again associated with the inorganic particles. Admittedly, W did pose some contrast issues due to a weak signal, however, there would seem to be little doubt of the

preferential adsorption of W onto the ZrC particles over the surrounding carbonaceous phase. We can thus conclude from these data that adsorption is attributable to the radiation tolerant ZrC phase.

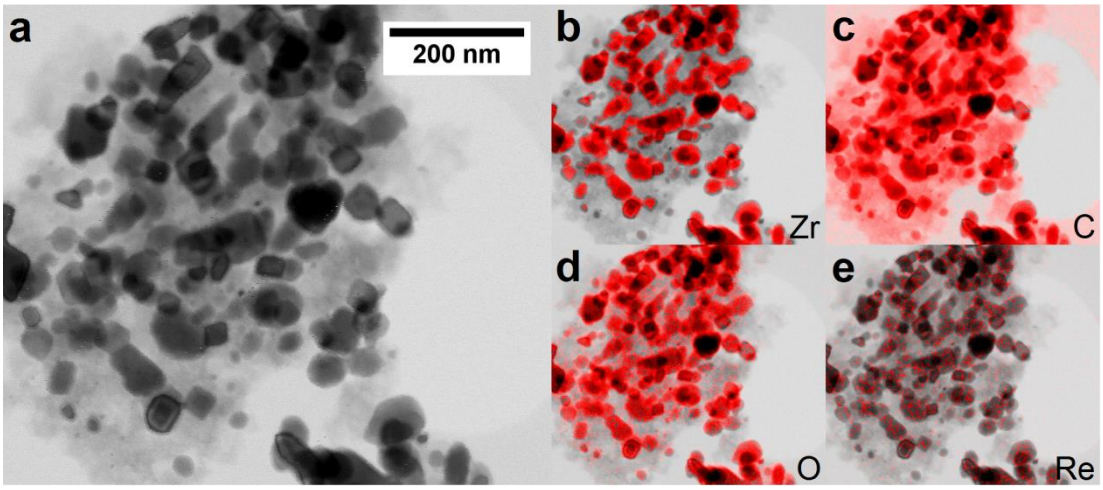

Figure 9 STEM studies of Re-loaded ZrAX-1. (a) Bright field image; and corresponding STEM-EDS elemental maps (b–e) of Zr, O, C and Re distributions.

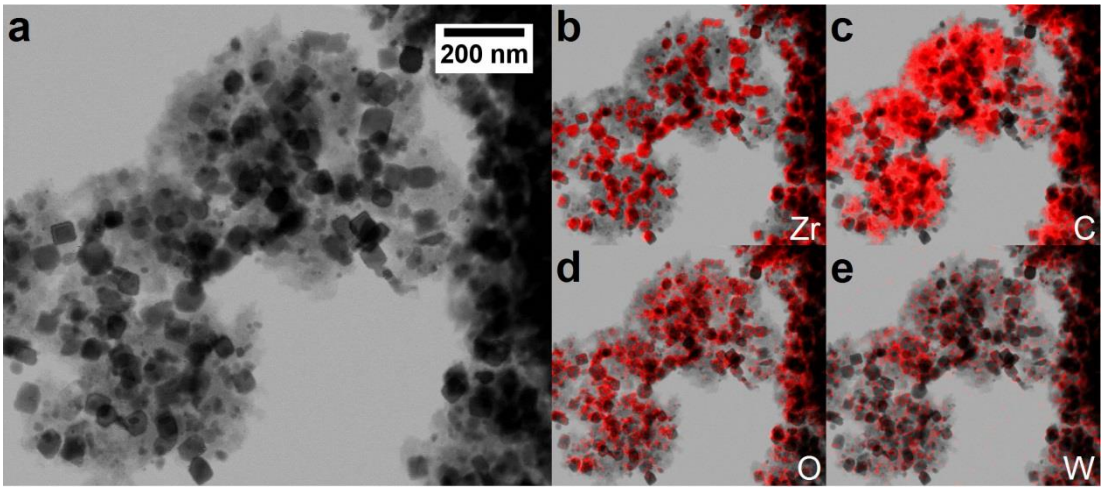

Figure 10 STEM studies of W-loaded ZrAX-1. (a) Bright field image; and corresponding STEM-EDS elemental maps (b–e) of Zr, O, C and W distributions.

4 Conclusions

We have reported new carbon-ZrC porous microspheres prepared by a facile procedure utilising ion-exchange of a Zr-oxalate complex into common polystyrene-divinylbenzene-based anion-exchange resins, with subsequent carbothermic treatment. The products were extremely robust, exhibiting high surface areas and generally contained mixtures of ZrC and ZrO_2 polymorphs ($tZrO_2$ and $mZrO_2$). However, one material (ZrAX-1), was demonstrated to be phase-pure ZrC and possessed the highest surface area of the series (448 $m^2\ g^{-1}$).

Some correlations were observed between the precursor morphologies and Zr loadings; and the crystalline phase compositions. High ZrC phase purity was seen in the macroporous resin-derived ZrAX-1, while the gel resin-derived materials did not exceed 20 wt% ZrC. It is possible that the open macroporous texture of ZrAX-1 may have aided the O removal kinetics. Also, ZrAX-1 was distinguished from the other carbothermal reduction products by its high Zr content of 52 wt%. It is also conceivable that the higher Zr loading in ZrAX-1 may have enhanced the conversion efficiency.

Evolution of the structure of ZrAX-1 was studied as a function of temperature. Tetragonal ZrO_2, already crystallised at 850 °C, underwent carbothermal reduction to form ZrC, which appeared from 1150 °C. By 1350 °C, the conversion was complete. The changes in porosity, surface area, crystallinity and carbon in-plane crystallite size together pointed to the origin of the high surface areas being as a result of reactive carbon removal.

Investigations of Re and W adsorption onto ZrAX-1 as a function of pH revealed high extraction of these elements over a wide pH range, suggesting credible use as irradiation hosts for the $^{188}W/^{188}Re$ system. Conceivably, the materials could also be applicable to production of ^{186}Re. The modelled W Langmuir adsorption capacity (49.54 mg g^{-1}) was much higher than the Re adsorption capacity (11.06 mg g^{-1}), seemingly by virtue of the cluster chemistry of the former. Elemental mapping demonstrated that the Re and W adsorption can be attributed to the embedded particles of the ZrC phase, which is known to be very radiation tolerant. The multi-modal pore sizes of ZrAX-1 should facilitate its use in a master generator for elution of the aforementioned nuclear medicine. However, the present results suggest that it is probably unlikely to be suitable in a point-of-use generator due to the much stronger binding of Re over W. Follow-up work, however, might conceivably establish conditions for the selective elution of Re.

Although the current scheme of irradiation and dissolution may not seem overly laborious, the materials presented in this work may help to simplify production of ^{188}W. For example, the ZrAX-1 microspheres could be packed into a Zr alloy column housing and loaded with the ^{186}W target nuclide by simple column chromatography. After irradiation, the ^{188}W product would then be readily eluted by passing strong alkali through the column. Following washing to remove the alkaline eluant, the column module could be reloaded with ^{186}W solution and the process repeated. Apart from the enhanced efficiency that such an approach would bring, the potential for lower occupational exposure of workers as a result of reduced active handling, may also be an advantage.

Acknowledgements

Materials and equipment access were provided and/or funded by Australian Nuclear Science and Technology Organisation (ANSTO). The authors gratefully acknowledge the following ANSTO staff for their contributions: Mr Kerry Cruikshank and Dr Ken Short for ongoing technical support for our tube furnace; Mr Karl Toppler for assistance with mechanical testing equipment; and Mr Joel Davis for SEM data. Mercury Porosimetry data were acquired by Particle & Surface Sciences Pty Ltd, NSW, Australia and O, N microanalysis was conducted by CSIRO Mineral Resources, VIC, Australia; both on a pay-per-sample basis. This research has been conducted with the support of the Australian Government Research Training Program Scholarship. Professor Chen acknowledges continuing support from Australian National Fabrication Facility (ANFF).

References

1. Dash A, Knapp FFRJ (2015) An overview of radioisotope separation technologies for development of 188W/188Re radionuclide generators providing 188Re to meet future research and clinical demands. RSC Advances 5:39012-39036
2. Yttrium-90 and Rhenium-188 radiopharmaceuticals for radionuclide therapy (2015). IAEA radioisotopes and radiopharmaceuticals series no. 5. International Atomic Energy Agency, Vienna
3. Argyrou M, Valassi A, Andreou M, Lyra M (2013) Rhenium-188 production in hospitals, by W-188/Re-188 generator, for easy use in radionuclide therapy. Int J Mol Imaging:290750. doi:10.1155/2013/290750
4. Katoh Y, Vasudevamurthy G, Nozawa T, Snead LL (2013) Properties of zirconium carbide for nuclear fuel applications. J Nucl Mater 441:718-742. doi:10.1016/j.jnucmat.2013.05.037

5. Snead LL, Katoh Y, Kondo S (2010) Effects of fast neutron irradiation on zirconium carbide. J Nucl Mater 399:200-207. doi:10.1016/j.jnucmat.2010.01.020
6. Scales N, Chen J, Hanley TL, Riley DP, Lumpkin GR, Luca V (2015) Hierarchically porous carbon-zirconium carbide spheres as potentially reusable transmutation targets. Microporous Mesoporous Mater 212:100-109. doi:10.1016/j.micromeso.2015.03.025
7. Scales N, Chen J, Aughterson RD, Karatchevtseva I, Stopic A, Lumpkin GR, Luca V (2018) Porous Zr2SC-carbon microspheres: Possible radiation tolerant sorbents and transmutation hosts for technetium-99. Microporous Mesoporous Mater 259:67-78
8. Bochkarev GS, Zaitsev LM, Kozhenkova VN (1963) Complexes of zirconium oxalates. Zh Neorg Khim 8:2248-2253
9. Simonits A, De Corte F, Hoste J (1975) Single-comparator methods in reactor neutron activation analysis. J Radioanal Chem 24 (1):31-46. doi:10.1007/BF02514380
10. Pimenta MA, Dresselhaus G, Dresselhaus MS, Cancado LG, Jorio A, Saito R (2007) Studying disorder in graphite-based systems by Raman spectroscopy. Phys Chem Chem Phys 9 (11):1276-1291. doi:10.1039/b613962k
11. Sing KSW, Everett DH, Haul RAW, Moscou L, Pierotti RA, Rouquerol J, Siemieniewska T (1985) Reporting physisorption data for gas/solid systems. Pure Appl Chem 57:603-619
12. Ferrari AC (2007) Raman spectroscopy of graphene and graphite: Disorder, electron-phonon coupling, doping and nonadiabatic effects. Solid State Commun 143 (1-2):47-57. doi:10.1016/j.ssc.2007.03.052
13. Baes CF, Mesmer RE (1976) The Hydrolysis of Cations. John Wiley and Sons, Inc., New York